

Phase diagram study of the formation and crystallization of Ge–metal amorphous alloy films

ZHANG RENJI

Department of Mechanical Engineering, Tsinghua University, Beijing, Peoples' Republic of China

LI LI

Department of Physics, Lanzhou University, Lanzhou, Peoples' Republic of China

WU ZIQIN

Centre of Fundamental Physics, University of Science and Technology of China, Hefei, Peoples' Republic of China

The Ge–Au and Ge–Ag alloy films were deposited in vacuum at room temperature and then systematically observed in the TEM. The maximum metallic concentrations in the alloy films, C_{\max} , which form the stable amorphous alloy phases of germanium with gold and silver, were obtained. The annealed crystallization temperature T_c , which falls with increasing metallic content in these films was also found. The structures of these films and their annealed specimens were also studied. There are various factors which influence the formation of amorphous alloy films deposited in vacuum for Ge–metal systems. A new formula for C_{\max} has been derived. The annealed crystallization character has been explained by means of the variation of the free energy and the activation energy of crystallization. The activation energy of crystallization, E_a , can be obtained from the data values of T_c . For Ge–Au films, $E_a(\text{Au}) = E_a^0 / (-18.66 C_{\text{Au}}^2 + 16.83 C_{\text{Au}} + 1) \pm 3.3$ (kcal mol⁻¹); for Ge–Ag films, $E_a(\text{Ag}) = E_a^0 / (-2.754 C_{\text{Ag}}^2 + 3.815 C_{\text{Ag}} + 1) \pm 2.6$ (kcal mol⁻¹). In order to explain all these results, two kinds of phase diagram for the alloy films have been introduced. One is the three-dimensional relationship diagrams of phase formation in semiconductor–metallic alloy films; it was introduced to explain the influencing factors. The other is the three-dimensional phase diagrams of annealed semiconductor–metallic films systems. From this diagram all the phase transitions can be found.

1. Introduction

The amorphous semiconductor (germanium or silicon)–metallic alloy films have important applications in the field of electronic devices, and the degeneration in this kind of thin film could occur during the operation process, so investigation of the formation of the amorphous state and the annealed crystallization of these films has great significance in practice [1–5]. Usually the Ge (or Si)–metallic co-deposited films which are rich in germanium (or silicon) can form the amorphous state. In this kind of film, germanium (or silicon) forms in the amorphous state during the co-deposition process at room temperature or lower temperature. Chopra *et al.* [6–13] investigated Ge–metallic alloy films and found that different metals have different maximum metallic concentrations, C_{\max} , which form stable and homogeneous amorphous alloy phases during the room-temperature deposition process. The experimental values of C_{\max} for different Ge–metallic systems were

obtained by Randhawa *et al.* [14–17]. Based on these results they derived a formula using some parameters expressing the properties of Ge–metallic systems

$$C_{\max} = A_0 \exp(-mT_m) + \sum_{j=0}^5 a_j S^j \quad (1)$$

where C_{\max} is in atomic per cent, T_m is the melting point of the metal (K), S is the solid solubility of metallic element in c-Ge at 500 °C (773 K) according to the equilibrium phase diagram (at %), A_0 , m and a_j ($j = 0-5$) are constants. The variation of the structure of the Ge (or Si)–metallic co-deposited films plays an important role in their applications due to the variation of their properties in many fields [18–23]. For example, because of the crystallization of the semiconductor-metal alloy films, the conductivity of the films changes to a great degree; it influences the electronic and optical properties of these films significantly [7, 10, 13, 24]. After the annealing treatment for

the Ge–Au and Ge–Ag amorphous films, the amorphous germanium (a-Ge) crystallized, and the crystallization temperature, T_c , decreases with increasing metallic content [9, 11, 25–30].

In the present work, systematic transmission electron microscope (TEM) observations and selected-area diffraction (SAD) analyses were made for Ge–Au and Ge–Ag co-deposited alloy films and their annealed films over wide concentration ranges. From TEM and SAD experiments, we found that the stable and homogeneous amorphous alloy films could form only at lower metallic contents ($C_{Au} \leq 16.6$ at %, $C_{Ag} \leq 3.4$ at %) for room-temperature deposition; the SAD patterns for these films indicated amorphous germanium (a-Ge) haloes. When the metallic contents were higher, the room-temperature deposited films were composed of Au–Ge metastable phase and a-Ge phase for the Ge–Au system and the SAD patterns were composed of Au–Ge metastable phase dotted rings and a-Ge haloes. On the other hand, the mixture of a-Ge and polycrystalline Ag (c-Ag) occurred for room-temperature deposition for the Ge–Ag system, the SAD pattern being composed of a-Ge haloes and c-Ag rings. The pure a-Ge film had $T_c = 450^\circ\text{C}$ (723 K) under our annealing conditions. Throughout the TEM and SAD experiments, the roles of the variation of T_c with metallic content and the formation of phases in the annealed films with different annealing temperature T_a were known. The factors which influence the formation of the amorphous alloy deposited films were estimated and a new formula using more parameters expressing the properties of the Ge–metallic systems was derived. The annealed crystallization is explained based on the variation of the free energy and the activation energy of the crystallization of a-Ge in the alloy films. The formulae for E_a varied with the metallic contents C_{Au} and C_{Ag} were derived based on the T_c values and the value of pure germanium film E_a^0 [31]. In order to describe these results two kinds of phase diagram of the alloy films were introduced: (1) three-dimensional phase formation diagram for describing the phase formation of the alloy films deposited in vacuum; (2) three-dimensional phase transition diagram for describing structural changes of the alloy films. Finally, a comparison of the crystallization mechanisms and the crystallization properties of the alloy films with semiconductor/metal bilayer films was made.

2. Experimental method

2.1. Specimen preparation

The alloy films were co-deposited on to freshly cleaved NaCl (1 00) crystal at room temperature. The distance between the evaporating source and the sheet surface was 60.0 mm. The deposition started at a pressure of 2.7×10^{-3} Pa. During the deposition process the pressure was about 6.7×10^{-3} Pa, the evaporation rate was about 2 nm s^{-1} , and the film thickness about 50 nm. Before deposition a shelter was placed on top of the sheet and the deposited materials were pre-fused three times with a small current in the tungsten boat. Nine concentrations were studied for each system. The

C_{Au} range was 2–80 wt % (0.75–60 at %) and the C_{Ag} range 2–75 wt % (1.4–67 at %). The concentration of each sample was obtained by weighing raw materials of the alloys and verifying the results by energy dispersive X-ray spectroscopy (EDX) analysis.

2.2. Specimen annealing

The annealing of the alloy films was carried out in the vacuum diffusion furnace. The specimens were sealed in the quartz tube. Before heating the pressure in the tube was 2.7×10^{-3} Pa. When the temperature in the furnace reached a given value, the quartz tube was moved into the constant-temperature region in the furnace. When the given temperature was re-obtained after the rapid rising of the temperature (in the duration of 2.5 min or less), the time was recorded. During annealing, the variation range in the temperature in the tube was less than $\pm 5^\circ\text{C}$. The pressure in the tube became lower than before the tube was moved into the constant-temperature region, but after maintaining the temperature for 1–2 min after the given temperature was obtained, the pressure in the tube again reached 2.7×10^{-3} Pa. The annealing treatment was continued for a certain time (usually 30 min), then the quartz tube was moved out off furnace cavity and cooled rapidly in cool water. After 1–3 min when the temperature in the tube had fallen to 30–40°C, the annealed specimen could be removed. A series of annealed specimens was made for the Ge–Au and Ge–Ag amorphous alloy films with different compositions, and annealing temperatures, T_a , from 50–500°C, at 50°C intervals.

2.3. TEM observation

TEM observation and SAD analysis were performed with a JEM-200CX scanning transmission electron microscope (STEM); the accelerating voltage was usually 200 kV. Because the crystallization behaviour of a-Ge film was influenced by the electron-beam radiation, the following experimental procedure was adopted: (1) the sample chamber was cooled with liquid nitrogen; (2) the intensity of the electron beam was maintained as small as possible; (3) whilst the electron beam irradiated one area of the film during the adjusting operation, it was moved to an other interesting area of the film adjacent to the initial area for microphotography; (4) micro-beam analysis was made with the EDAX 9100 X-ray EDS attached to the STEM. Because the illumination time of the electron beam was as long as 2 min during composition analysis, this must be the final step. In the experimental process, the correspondence between the microphotograph, microdiffraction and microanalysis must be guaranteed [32–34], although the area of micro-analysis was larger than that of the microdiffraction.

3. Experimental results

3.1. Alloy films deposited at room temperature

The concentration range of the nine Ge–Au films ranged from 2–80 wt % (0.75–60 at %). That of the

TABLE I Composition and TEM observations of Ge-Au alloy films deposited at room temperature

Film no.	1	2	3	4	5	6	7	8	9
C_{Au} (at%)	2	5	10	15	25	35	50	65	80
(wt%)	0.75	1.9	3.9	6.1	10.9	16.6	26.9	40.6	59.6
TEM	No grain appears	No grain appears	No grain appears	No grain appears	No grain appears	$D \sim 10$ nm $\rho \sim 1 \times 10^9$ mm ⁻²	$D \sim 15$ nm Film segregation occurs	Film is divided into segregation region and radiative stripe region (diameter ~ 25 μ m)	Lamellar structure forms, width of layer ~ 25 nm length of layer ~ 0.2 μ m
SAD	a-Ge haloes	a-Ge haloes	a-Ge haloes	a-Ge haloes	a-Ge haloes	a-Ge haloes + Au(111)	a-Ge rings + Au-Ge metastable phase dotted rings	Au-Ge metastable phase dotted rings + a-Ge rings	Au-Ge metastable phase dotted rings

TABLE II Composition and TEM observations of Ge-Ag alloy films deposited at room temperature

Film no.	1	2	3	4	5	6	7	8	9	
C_{Ag} (at%)	2	5	10	15	25	35	50	65	75	
(wt%)	1.4	3.4	7.0	10.6	18.3	26.6	40.2	55.6	66.9	
TEM	No grain appears	$D \leq 10$ nm $\rho \sim 0.5 \times 10^9$ mm ⁻²	$D \leq 10$ nm $\rho \sim 2 \times 10^9$ mm ⁻²	$D \sim 10$ nm $\rho \sim 2.5 \times 10^9$ mm ⁻²	$D \sim 10$ nm $\rho \sim 2.5 \times 10^9$ mm ⁻²	$D \sim 15$ nm $\rho \sim 3 \times 10^9$ mm ⁻²	$D \sim 15$ nm $\rho \sim 3 \times 10^9$ mm ⁻²	$D \sim 20$ nm $\rho \sim 4 \times 10^9$ mm ⁻²	$D \sim 20$ nm $\rho \sim 4 \times 10^9$ mm ⁻²	$D \sim 20$ nm $\rho \sim 4 \times 10^9$ mm ⁻²
SAD	a-Ge haloes	a-Ge haloes + Ag(111)	a-Ge haloes + Ag(111)	a-Ge haloes + Ag(111)	a-Ge haloes + c-Ag rings	a-Ge haloes + c-Ag rings	a-Ge haloes + c-Ag rings	a-Ge haloes + c-Ag rings	a-Ge haloes + c-Ag rings	

nine Ge–Ag films was 2–75 wt % (1.4–67 at %). Tables I and II present the main results of the room-temperature observations for Ge–Au and Ge–Ag films, respectively. Figs 1 and 2 show micrographs and the SAD patterns of four of the nine films, respectively. From Tables I and II and Figs 1 and 2 the following observations may be made.

1. There are no obvious grains in the photographs and the film has a homogeneous amorphous structure for $C_{Au} < 25$ wt % (11 at %) and $C_{Ag} < 2$ wt % (1.4 at %); the SAD patterns consist of a-Ge haloes.

2. There are very fine grains in the photographs when $C_{Au} = 35$ wt % (17 at %) and $C_{Ag} = 5$ wt % (2.4 at %), their size being about 10 nm or even smaller. The Au (1 1 1) and Ag (1 1 1) rings appear in the SAD patterns. It is shown that some of the Au(Ag) atoms are present as Au(Ag) clusters under our experimental conditions. However, Randhawa *et al.* [14–17] discovered that the largest content of silver which could form the homogeneous amorphous phase deposited at room temperature for the Ge–Ag alloy system was $C_{Ag(max)} = 12$ at %. This difference is

based on the experimental conditions. Because the formation of a mixed phase of germanium and silver is more difficult than that of germanium and gold, silver forms the finer grains on the NaCl monocrystalline substrate.

3. In addition to the a-Ge haloes Au–Ge metastable phase dotted rings appear in the SAD pattern [35–37] when $C_{Au} = 50$ wt % (27 at %). This shows that the Au–Ge metastable phase forms easily under room-temperature deposition in a vacuum, but excess germanium is still in the amorphous state. From the micrograph it is seen that the film is not homogeneous.

The a-Ge haloes are weaker and the Au–Ge metastable phase dotted rings are stronger in the SAD pattern at $C_{Au} = 65$ wt % (41 at %). There are some radially striped regions in the film; the diameter of these regions is about 2.5 μ m.

Only the Au–Ge metastable phase dotted rings are seen in the SAD pattern for $C_{Au} = 80$ wt % (60 at %). It is known that there is no a-Ge present. The film has the layer structure which is observed in the micrographs, and their morphology is very similar to that of

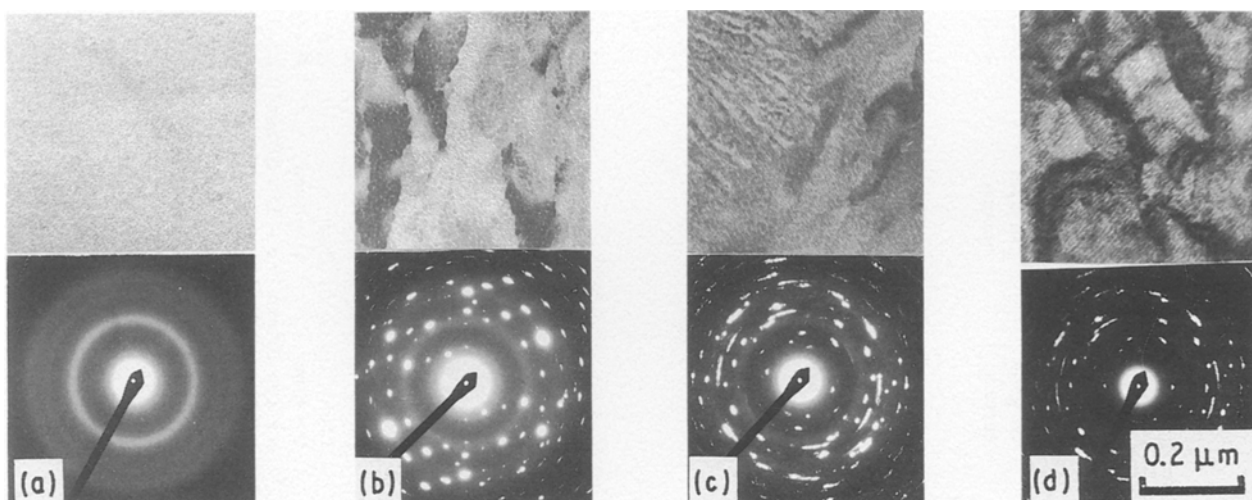


Figure 1 The room-temperature observation of Ge–Au alloy films. (a) 35 wt % Au, (b) 50 wt % Au, (c) 65 wt % Au, (d) 80 wt % Au.

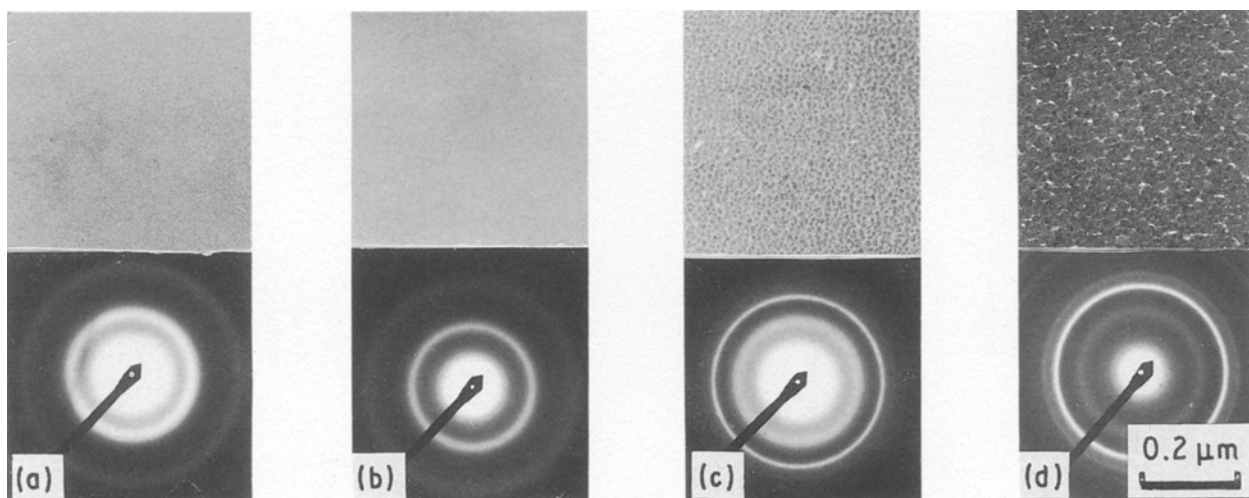


Figure 2 The room-temperature observation of Ge–Ag alloy films. (a) 2 wt % Ag, (b) 5 wt % Ag, (c) 25 wt % Ag, (d) 65 wt % Ag.

TABLE III The determination of crystallization temperature, T_c , from annealing samples of Ge-Au alloy films

Film no.	1	2	3	4	5	6	7	8	9
C_{Au} (at%)	2	5	10	15	25	35	50	65	80
(wt%)	0.75	1.9	3.9	6.1	10.9	16.6	26.9	40.6	59.6
T_c (°C)	400-450	250-300	200-250	150-200	100-150	50-100	20-50	20-50	20-50
Non-crystallized films T_a (°C)	No grain appears								
TEM	a-Ge haloes	5-20 nm grains appear	5-10 nm grains appear	5-10 nm grains appear	5-10 nm grains appear	5-10 nm grains appear	5-10 nm grains appear	5-10 nm grains appear	5-10 nm grains appear
SAD	a-Ge haloes	a-Ge haloes	a-Ge haloes	a-Ge haloes + Au(111)	a-Ge haloes + Au(111)	a-Ge haloes + Au(111)	a-Ge haloes + c-Au ring. New rings are between Au(111),(200)	a-Ge haloes + c-Au ring. New rings are between Au(111),(200)	a-Ge haloes + c-Au ring. New rings are between Au(111),(200)
Crystallized films T_a (°C)	450	300	250	200	150	100	50	50	50
TEM	$D \sim 10$ nm	$D \sim 10$ nm	$D \sim 10$ nm	$D \sim 10$ nm	$D \sim 10$ nm	$D \sim 15$ nm	White region $D \sim 30$ nm; black region $D \sim 15$ nm	White region $D \sim 50$ nm; black region $D \sim 25$ nm	Similar to eutectic stripped structure, widths: white ~ 20 nm, black ~ 30 nm
SAD	c-Ge rings	c-Ge rings + Au(111)	c-Ge rings + Au(111)	c-Ge rings + Au(111)	c-Ge rings + Au(111)	c-Ge rings + Au(111)	(c-Ge + c-Au) rings. New dotted rings are between Au(111), Ge(220)	(c-Ge + c-Au) rings. New dotted rings are between Au(111), Ge(220)	(c-Ge + c-Au) rings. New dotted rings are between Au(111), Ge(220)

TABLE IV Systematic TEM observations of annealed samples of Ge–Au films

Film no.	2	5	6	9
C_{Au} (wt %)	5	25	35	80
(at %)	1.9	10.9	16.6	59.6
T_c (°C)	250–300	100–150	50–100	20–50
T_a (°C)				
TEM	300	150	100	~15
	350	200	150	~18
	400	250	200	~20
	450	300	250	~25
	500	350	300	~30
	500 °C film has big black grains about 40–60 nm	400	350	~35
		450	400	~40
		500	450	~45
			500	{ white ~80 { black ~40
				D(nm) T_a (°C) white black 300 ~120 ~30 350 ~200 ~50 400 °C film: recrystallization after melting
SAD	300–450 °C films: c-Ge rings, Au(111) can be seen faintly. 500 °C film: c-Ge continued dotted rings + Au(111) (more obvious than before), there are weak rings between Au(111) and Ge(220)	150–350 °C films: c-Ge c-Ge rings + Au(111). 400–500 °C films: (c-Ge + c-Au) continued dotted rings. 400–450 °C films: there are new dotted rings between Au(111) and Ge(220). 500 °C film: new rings become very weak	100–200 °C films: (c-Ge + c-Au) rings. 250–450 °C films: (c-Ge + c-Au) continued dotted rings. 500 °C film: (c-Ge + c-Au) discontinued dotted rings. 100–250 °C films: the dotted rings between Au(111) and Ge(220) disappear. 300–500 °C films: there are new dotted rings between Au(111) and Ge(220) (very weak)	50–350 °C films: (c-Au + c-Ge) dotted rings + dotted rings between Au(111) and Ge(220), last rings are weakened in 250 °C film and disappear in 300–350 °C films basically. 400 °C film: (c-Au + c-Ge) big dotted rings

the layer structure of the Au–Ge eutectic alloy. The width of each layer is about 25 nm and its length is about 0.2 μ m.

4. With increasing silver content the mean grain density in the films increases, together with the mean grain size. The SAD pattern shows that the film is composed of a-Ge and silver grains. When C_{Ag} is small, the a-Ge haloes and the Ag(111) ring are present in the SAD pattern; as C_{Ag} increases the other c-Ag rings gradually appear. When $C_{Ag} = 75$ wt % (67 at %), the a-Ge haloes become very weak.

3.2. Annealed alloy films

The TEM observation and SAD analysis results for different kinds of annealed Ge–Au films are presented in Tables III and IV and Figs 3 and 4; those for Ge–Ag films are given in Tables V and VI and Fig. 5.

1. The Ge–Au amorphous alloy film which had lower gold contents, $C_{Au} < 35$ wt % (17 at %), crystallized at a given annealing temperature. When $C_{Au} = 2$ wt % (0.75 at %), $T_c = 400$ –450 °C (673–723 K). T_c decreases with increase in C_{Au} . When $C_{Au} = 25$ wt % (11 at %), $T_c = 100$ –150 °C (373–423 K) (Table III). With $C_{Au} = 5$ wt % (2 at %), only a few grains present had a diameter of 5–20 nm for $T_a = 250$ °C (523 K), but many small grains (grain diameter $D \approx 10$ nm) appear in the $T_a = 300$ °C

(573 K) film (see Fig. 3a, b); only a-Ge haloes are seen in the SAD pattern for 250 °C (523 K) film, but c-Ge rings and a very weak Au(111) ring appear for the 300 °C (573 K) film (Tables III and IV). For the Ge–25 wt % (11 at %) Au alloy film, there are the similar variations in different T_a films (see Fig. 3c, d). $D = 5$ –10 nm in the 100 °C (373 K) film, the mean grain size being up to 10 nm when the film is annealed at $T_a = 150$ °C (423 K); a-Ge crystallized at the same time. For a higher T_a [≥ 200 °C, (473 K)], D gradually increases with T_a ; when $T_a = 500$ °C (773 K), $D \sim 30$ nm (Table IV). It is shown that the metallic grains appear at the beginning of crystallization process of the amorphous alloy films for Ge–Au films ($C_{Au} < 35$ wt % (17 at %)).

2. When the gold content increases to 35 wt % (17 at %) in the alloy films, the dotted diffraction rings of the Au–Ge metastable phase appear in the SAD pattern for the 50 °C (323 K) film (Table III). Coincident with this report [25, 26] is that the stage of the germanium (or silicon)-metallic metastable phase formation usually occurs before crystallization of the a-Ge (or silicon) in the germanium (or silicon)-metal alloy films. On annealing at 100 °C (373 K), the crystallization of a-Ge occurs, and the rings of the metastable phase disappear from the SAD pattern at the same time.

TABLE V Determination of crystallization temperature, T_c , from annealed samples of Ge-Ag alloy films

Film no.	1	2	3	4	5	6	7	8	9
C_{Ag} (wt%)	2	5	10	15	25	35	50	65	75
(at%)	1.4	3.4	7.0	10.6	18.3	26.6	40.2	55.6	66.9
T_c (°C)	450-500	350-400	300-350	300-350	250-300	200-250	150-200	150-200	150-200
Non-crystallized film T_d (°C)	450	350	300	300	250	200	150	150	150
TEM	No grain appears	$D \sim 15$ nm	$D \sim 15$ nm	$D \sim 15$ nm	$D \sim 25$ nm	$D \sim 20$ nm	$D \sim 30$ nm, divided into white and black regions first	$D \sim 30$ nm, divided into white and black regions first	$D \sim 80$ nm, divided into white and black regions first
SAD	a-Ge haloes	a-Ge haloes + Ag(111)	a-Ge haloes + Ag(111)	a-Ge haloes + Ag(111)	a-Ge haloes + c-Ag rings. Weak dotted rings are between Ag(111),(200)	a-Ge haloes + c-Ag rings	a-Ge haloes + c-Ag rings. New dotted rings are between Ag(111),(200)	a-Ge haloes + c-Ag rings. New dotted rings are between Ag(111),(200)	a-Ge haloes + c-Ag rings. New dotted rings are between Ag(111),(200)
Crystallized film T_d (°C)	500	400	350	350	300	250	200	200	200
TEM	$D \sim 10$ nm	$D \sim 20$ nm	$D \sim 18$ nm	$D \sim 20$ nm	$D \sim 35$ nm Black grains contact each other	$D \sim 25$ nm	$D \sim 35$ nm White and black regions separate further	$D \sim 40$ nm White and black regions separate further	$D \sim 90$ nm White region grows
SAD	c-Ge rings	c-Ge rings + Ag(111)	c-Ge rings + Ag(111)	c-Ge rings + Ag(111)	(c-Ge + c-Ag) rings. Very worn rings are between Ag(111),(200)	(c-Ge + c-Ag) rings. New rings are between	(c-Ge + c-Ag) rings. New dotted rings are between Ge(111), Ag(111)	(c-Ge + c-Ag) rings. New dotted rings are between Ge(111), Ag(111)	c-Ag rings + c-Ge rings (weak). New dotted rings are between Ge(111), Ag(111)

TABLE VI Systematic TEM observations of annealed samples of Ge-Ag films

Film no.	2	5	7	9
C_{Ag} (wt%)	5	25	50	75
(at%)	3.4	18.3	40.2	66.9
T_c (°C)	350-400	250-300	150-200	150-200
Non-crystallized film				
TEM	T_a (°C) D(nm)	T_a (°C) D(nm)	T_a (°C) D(nm)	T_a (°C) D(nm)
	100 ~ 10	100 ~ 20	100 ~ 25	100 ~ 70
	150 ~ 10	150 ~ 20	150 ~ 30	150 ~ 80
	200 ~ 10	200 ~ 20	There are some black grains at 100 °C.	There are big black grains at (0.5-1 μm) at 100 °C. The white regions appear at 150 °C
	250 ~ 12	250 ~ 25	150 °C film has white grains	
	300 ~ 12	There are some black grains at 100 °C		
	350 ~ 15			
SAD	a-Ge halo rings + Ag (1 1 1)	a-Ge halo rings + c-Ag rings. 100 °C film: new rings appear between Ag(1 1 1) and (2 0 0), when T_a is increased, new rings become weaker and weaker	a-Ge halo rings + c-Ag rings. 100 °C film: new rings appear between Ag(1 1 1) and (2 0 0), when T_a is increased, new rings become weaker and weaker	a-Ge halo rings + c-Ag rings. 100 °C film: new rings appear between Ag(1 1 1) and (2 0 0), when T_a is increased, new rings become weaker and weaker
Crystallized film				
TEM	T_a (°C) D(nm)			
	400 ~ 20	300 °C film: black grains ($D \sim 35$ nm) contact each other, film starts to divide into white and black regions, they separate further as T_a increases	200 °C film: black grains ($D \sim 35$ nm) contact each other, film starts to divide into white and black regions, they separate further as T_a increases	From 200 °C, the separation of white and black regions is further and further and white region grows gradually as T_a is increased. 500 °C film: big black grains ($D \sim 2$ μm) appear
	450 ~ 20			
	500 ~ 25			
SAD	c-Ge rings + Ag(1 1 1).	300 °C film: (c-Ge + c-Ag) rings, there are very weak rings between Ag(1 1 1) and Ge(2 2 0). 350 °C film: above rings disappear. 450-500 °C films: (c-Ge + c-Ag) dotted rings, there are new weak dotted rings within Ge(1 1 1) and Ag(1 1 1)	300 °C film: (c-Ge + c-Ag) rings, there are new dotted rings within Ge(1 1 1) and Ag(1 1 1). After T_a 350 °C c-Ag rings gradually weaken	300 °C film: c-Ge rings (weak) + c-Ag rings, there are new dotted rings within Ge(1 1 1) and Ag(1 1 1). After T_a 350 °C, c-Ag rings gradually weaken

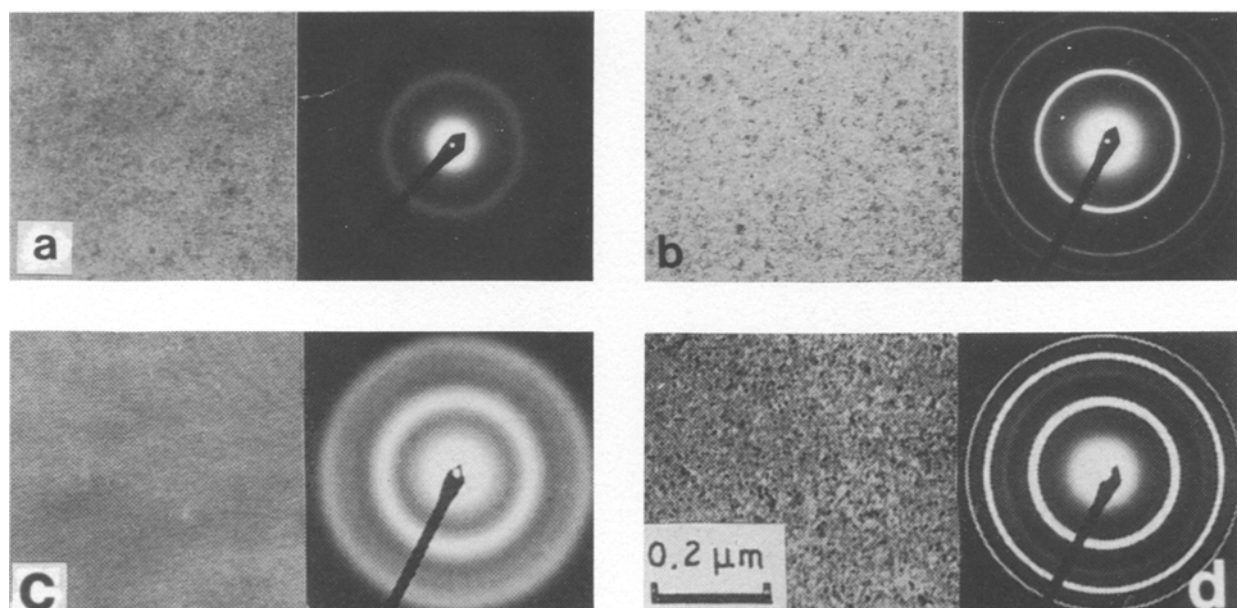


Figure 3 TEM observation of Ge-Au annealed films which had lower gold contents. (a, b) Alloy film of 5 wt % Au: (a) 250 °C, 30 min; (b) 300 °C, 30 min. (c, d) Alloy film of 25 wt % Au: (c) 100 °C, 30 min, (d) 150 °C, 30 min.

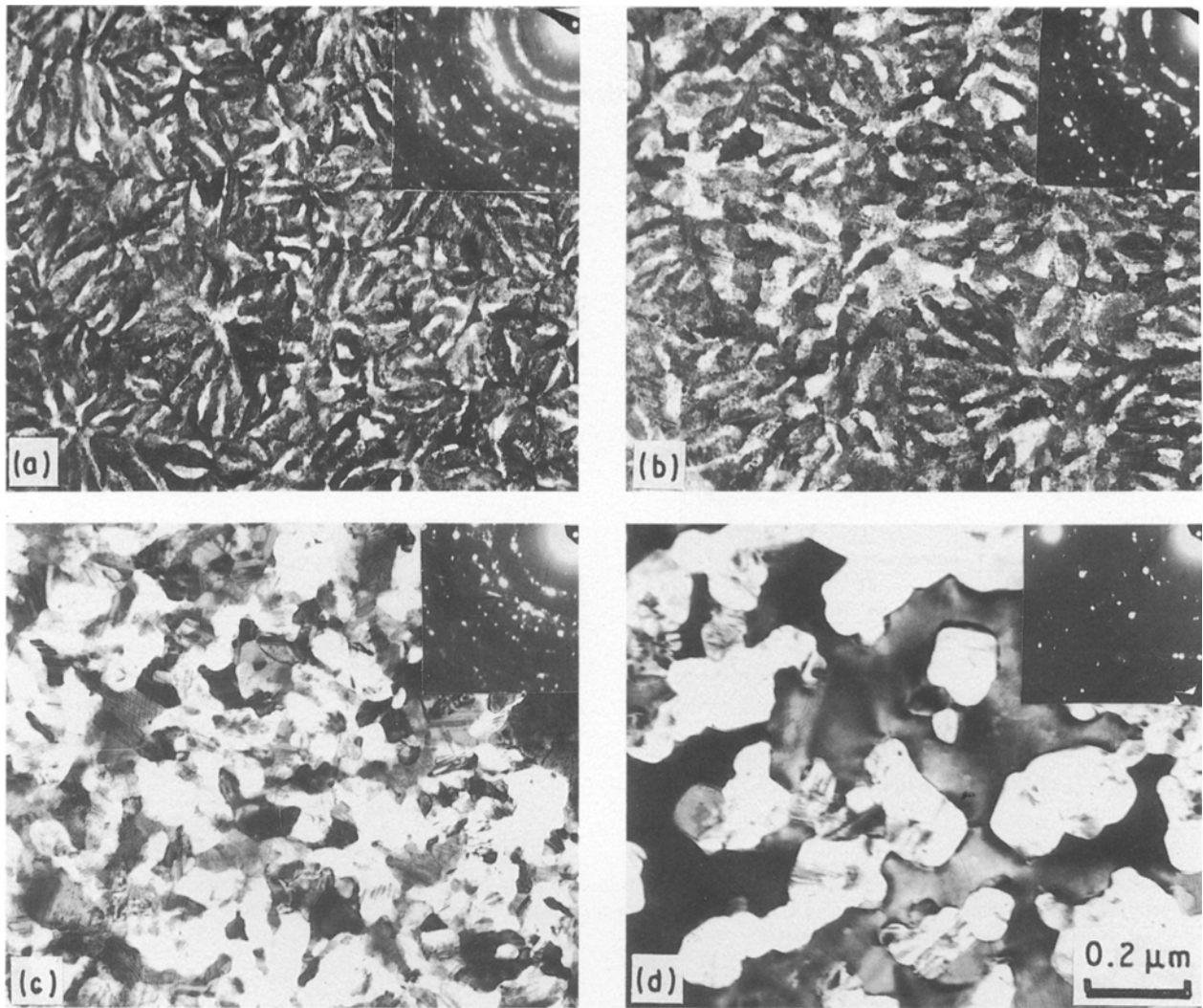


Figure 4 TEM observation of Ge-80 wt% Au annealed film. (a) 50 °C, 30 min, (b) 200 °C, 30 min, (c) 300 °C, 30 min, (d) 400 °C, 30 min.

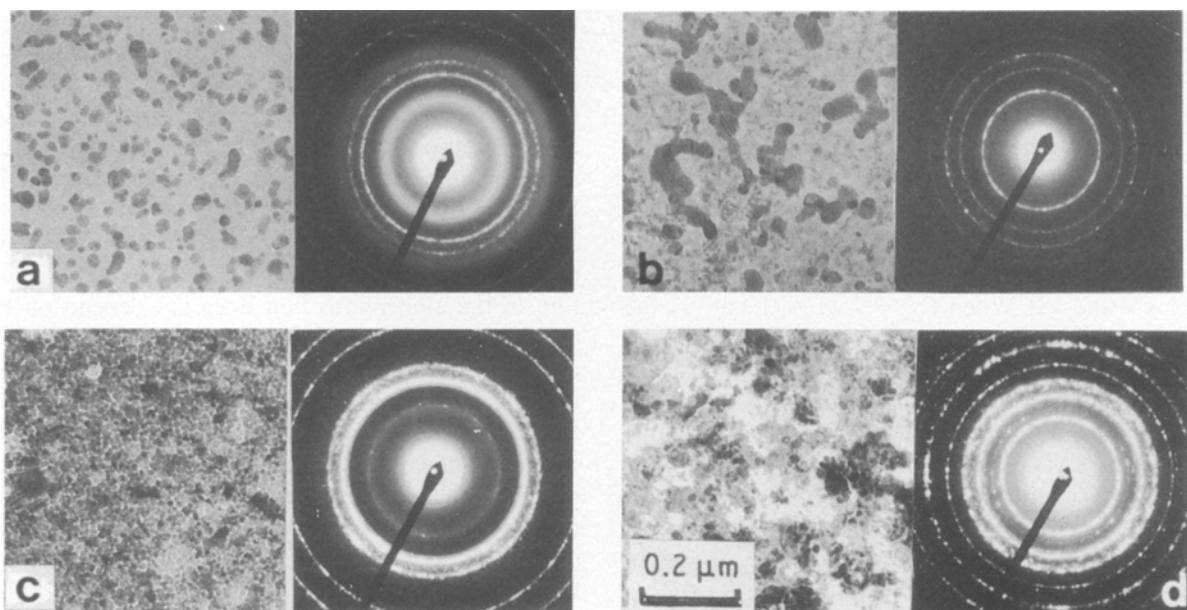


Figure 5 TEM observation of Ge-Ag annealed films. (a, b) 25 wt% Ag film, (a) 250 °C, 30 min, (b) 300 °C, 30 min. (c, d) 75 wt% Ag film, (c) 150 °C, 30 min, (d) 200 °C, 30 min.

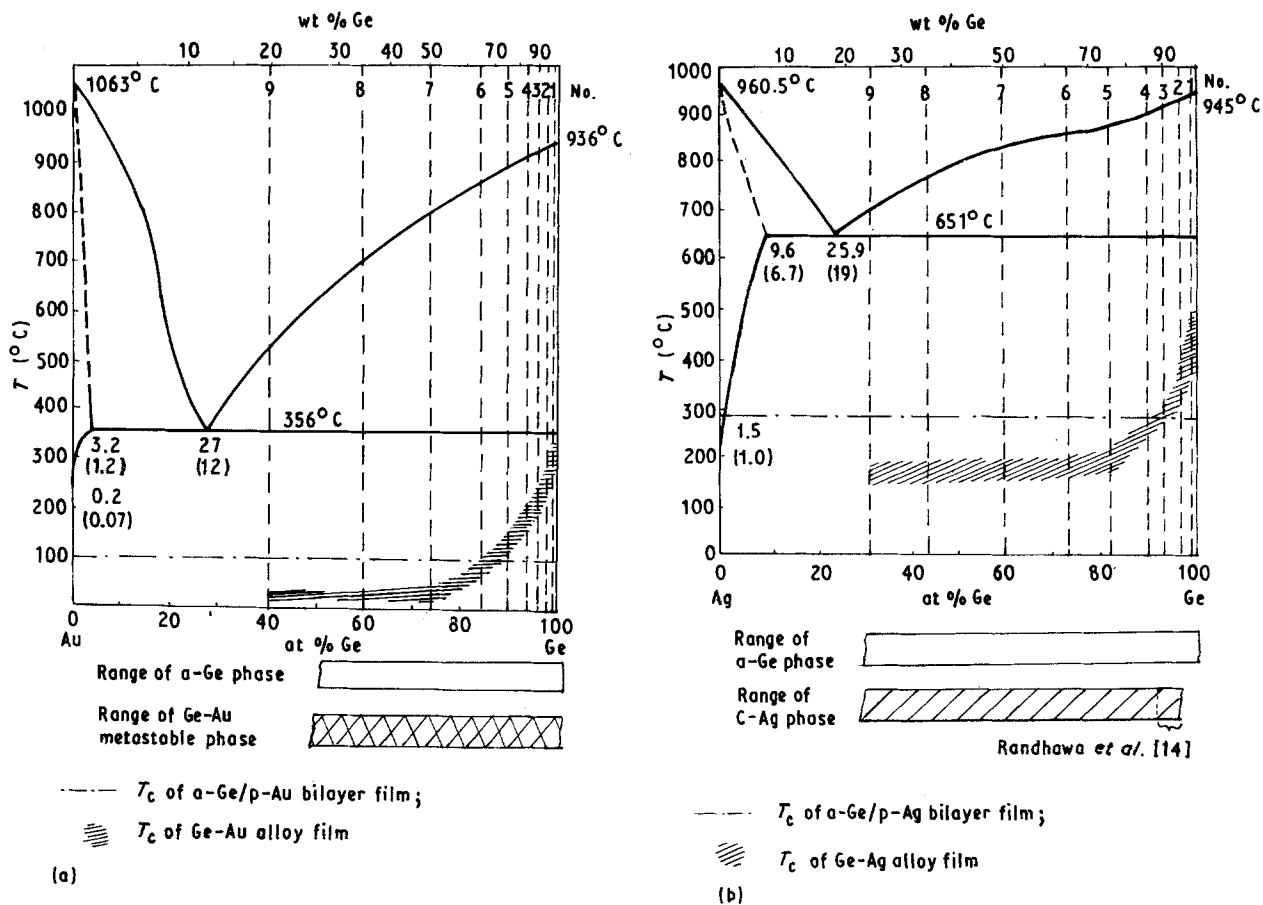


Figure 6 Ge-metallic element phase diagram. The concentration of each alloy film, the concentration range of each phase for room-temperature deposited films, the variation of crystallization temperature with concentration in alloy films and the a-Ge crystallization temperature in a-Ge/metal bilayer films, are marked.

3. When C_{Au} increases up to 50 wt % (27 at %), the Au-Ge metastable phase is found in the room-temperature deposited alloy film. When $T_a = 50^\circ\text{C}$ (323 K), the crystallization of a-Ge in the alloy film had begun, but the Au-Ge metastable phase also remains. The Au-Ge metastable phase disappears gradually as T_a increases. This is proved from the SAD patterns for different T_a annealed films (Table III). Fig. 4 shows the TEM observation for Ge-80 wt % (60 at %) Au film. During 50°C (323 K) annealing, the structure of the alloy film transforms from the layer structure to the eutectic lamellar structure; but during 300°C (573 K) annealing, the annealed film is composed of black and white regions. It is shown that the alloy film is melted during the high-temperature annealing period.

4. With increasing silver contents, the T_c for the Ge-Ag alloy films deposited in vacuum decreases (Tables V and VI). When $C_{Ag} = 2$ wt % (1.4 at %), the value of T_c is equal to that of the pure a-Ge film. When C_{Ag} increases up to 25 wt % (18 at %), the grain size D of the 100°C (373 K) annealed film is about 20 nm, and there are dotted rings of the Ag-Ge metastable phase in the SAD pattern (Table VI and Fig. 5a, b). As T_a is raised, the intensity of these dotted rings gradually decreases. The a-Ge in the 300°C (573 K) film has already crystallized, and the alloy film is composed of black and white regions (see Fig. 5). The annealing property of the Ge-Ag alloy films which have higher silver contents is the same as in this alloy film, the only difference being decrease in T_c (Figs 5c,d).

4. Discussion of the formation and crystallization of Ge-metallic alloy films

4.1. Factors which influence the formation of amorphous alloy films deposited at room temperature

Fig. 6 shows the Au-Ge and the Ag-Ge equilibrium phase diagrams. The concentration of each alloy film and also the concentration range for each phase at room temperature in each film are marked in the figure. The variation of the range of the a-Ge crystallization temperature with concentration of the alloy films are also shown [25, 26]. For comparison, the a-Ge crystallization temperatures in a-Ge/metal bilayer films are also given [25, 26].

In the usual vacuum-deposition conditions, because of the high supersaturation, judgement of the formation of the amorphous film does not depend on the classical theory of nucleation and growth of grains. In order to investigate the factors which influence the formation of amorphous alloy films deposited at room temperature in vacuum, Table VII gives details for some Ge-metallic systems. In addition to the main properties which influence the formation of the alloy, the C_{max} of each Ge-metallic system are also given (obtained by Randhawa et al. [14-17]). Although Randhawa et al. gave a formula of C_{max} (see Equation 1), they could not explain why only T_m (metallic melting point) and S (solid solubility of metal in c-Ge) can influence the value of C_{max} , the physical

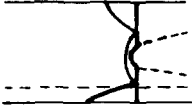
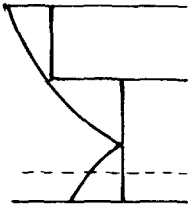
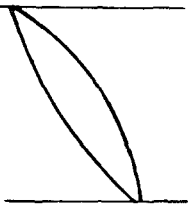
TABLE VII C_{\max} of Ge-metal co-deposited films and relative properties of metallic element

Z	C_{\max} (at %)	Group	Atomic size (nm)	Electro- negativity (P_e)	Melting point (K)	Solid solubility at 773 K (at %)	Crystalline structure	Eutectic Temp. (K)	Ge-metallic equilibrium phase diagram
32	Ge	IVA	2.788	1.8	1209		Diamond		
49	In	IIIA	3.14	1.7	429	0.5	Tetragonal	429	
31	Ga	IIIA	2.70	1.6	303	2.1	Rhombic	302.8	
47	Ag	IB	2.883	1.9	1233	10^{-6}	fcc	924	
79	Au	IB	2.878	2.4	1336	Negligible	fcc	629	
29	Cu	IB	2.551	1.9	1356	10^{-4}	fcc	913	

TABLE VII Continued

Z	C_{\max} (at %)	Group	Atomic size (nm)	Electro- negativity (P_e)	Melting point (K)	Solid solubility at 773 K (at %)	Crystalline structure	Eutectic Temp. (K)	Ge-metallic equilibrium phase diagram
83	20	VA	3.64	1.9	544	2.0	Trigonal	544	
13	30	IIIA	2.86	1.5	933	3-4	fcc	697	
28	30	VIIIB	2.49	1.8	1726	10^{-4}	High T: fcc low T: bcc	1048	
50	30	IVA	3.16	1.8	505	17	High T: tetragonal low T: diamond	505	
51	30	VA	3.22	1.9	903	3.0	Trigonal	863	

TABLE VII Continued

Z	C_{\max} (at %)	Group	Atomic size (nm)	Electro- negativity (P_e)	Melting point (K)	Solid solubility at 773 K (at %)	Crystalline structure	Eutectic Temp. (K)	Ge-metallic equilibrium phase diagram
26	40	VIII B	2.52	1.8	1808	10^{-4}	High T : fcc low T : bcc	1123	
<i>Ge-semiconductor co-deposited films</i>									
52	85	VIA	2.86	2.1	723				
14	100	IVA	2.35	1.9	1683				

meaning was not very clear. From Table VII the qualitative roles of the formation of the amorphous alloy films under co-deposition conditions at room temperature can be listed as follows.

1. A high solid solubility of metal in c-Ge.
2. A large difference in the electronegativity between metal and germanium.
3. A large difference in the atomic sizes between metal and germanium.
4. Low melting point of the metal.

From the equilibrium phase diagram scheme in Table VII it can be seen that the metallic elements which form an amorphous alloy film when co-deposited with germanium are: (1) a deep eutectic in the phase diagram of Ge-metallic system (Ge-Au, Ge-Ag, Ge-Cu, Ge-Fe, Ge-Ni, Ge-Al and Ge-Sb), or (2) a degenerate eutectic system, i.e. the so-called "eutectic" point was moved to the pure metallic side (Ge-In, Ge-Bi, Ge-Ga and Ge-Sn). The Ge-Te and Ge-Si systems are also included in Table VII, although tellurium and silicon are semiconductors. Their C_{\max} are higher at 85 at % (Ge-Te) or even near 100 at % (Ge-Si). Turnbull and co-workers [40-43] pointed out that because the liquid eutectic alloy has a high viscosity at relatively low temperatures it is favourable for solidification to a non-crystalline phase. Thus this type of Ge-metallic system is favourable for the formation of an amorphous alloy film because of the low atomic diffusibility when atoms arrive on a cold substrate during the deposition process.

Based on the above analysis, a new formula for C_{\max} has been derived to describe the relationship between the structural property and other main properties (including structural, physical and chemical properties) for Ge-metallic systems

$$C_{\max} = A_1[r(\text{Me}) - r(\text{Ge})]^2 + B_1[P_e(\text{Me}) - P_e(\text{Ge})]^2 + C_1[T_m(\text{Me}) - T_m(\text{Ge})]^2 + D_1S_d + E_1 \quad (2)$$

where r is the atomic radius (nm), P_e the electronegativity, T_m the melting point (K), S_d the solid solubility of metal in c-Ge at 500°C (773 K) in the equilibrium phase diagram (at %), and A_1 , B_1 , C_1 , D_1 and E_1 are empirical constants. There is a good coincidence between the calculated values with Equation 2 and the experimental values, if we let $A_1 = 20.45$, $B_1 = 152.5$, $C_1 = -11.88$, $D_1 = 0.02402$, and $E_1 = 1.574$.

4.2. Variation of the free energy during the crystallization of Ge-metallic amorphous alloy films deposited in vacuum

Fig. 7 shows a schematic diagram of the free energy curve of the Ge-Au (or Ge-Ag) system at a certain environmental temperature, T (for example, room temperature). When the film is deposited at room temperature, if the metallic content, C_{Me} , is low enough, the amorphous alloy film is formed. At that moment, the free energy curve is just at the position of a-Ge phase in Fig. 7; if the metallic content is higher,

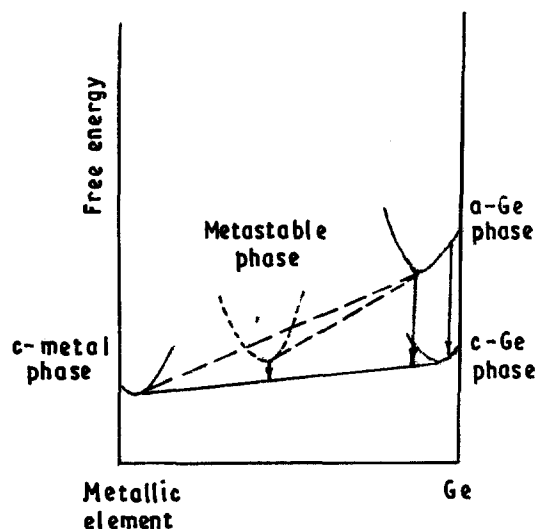


Figure 7 The schematic diagram of the free energy curves of vacuum-deposited films of the Ge-metallic system.

the film is then composed of the amorphous alloy phase and the crystalline metallic phase, and the proportion of these two phases is determined by the thermodynamical and dynamical factors during film formation. In the situation of the occurrence of the metastable phase, the film is composed of the amorphous alloy phase and the metastable phase (or the metastable phase plus the crystalline metallic phase, which depends on the relative positions of the free energy curves for these phases). Thus the concentration of the film determines the phases formed during vacuum deposition.

During the annealing process, the amorphous alloy films could crystallize, depending on the free energy condition of the alloy system. If the annealing temperature, T_a , is high enough to accelerate germanium atoms to overcome the crystallization barrier, a-Ge transforms into c-Ge and relieves the crystallization latent heat at the same time. From Fig. 7 it can be seen that the free energy of the alloy system decreases to the dynamical stable state during crystallization. When the room-temperature deposition film is composed of the Au-Ge (or Ag-Ge) metastable phase and a-Ge phase, on annealing, on the one hand, the Au-Ge (or Ag-Ge) metastable phase dissolves into c-Au + c-Ge (or c-Ag + c-Ge); on the other hand, a-Ge transforms into c-Ge, and then the total free energy of the alloy system decreases, so the dynamical stable state is obtained.

Fig. 8 is a schematic representation of the variation of the free energy of the Ge-metallic amorphous alloy phase in the Ge-metal film, with the metallic content. From this figure we have found that as the metallic content rises, the free energy of the system also increases, which is related to the free energy of the stable crystalline state, then the crystallization barrier which needs to be overcome during crystallization process is lower, so that the crystallization temperature T_c too is lower. When the metallic content C_{Me} is high enough (at that moment it just corresponds to the A''' line in Fig. 8), it is not possible to form the amorphous alloy film; only the crystalline film could form during room-temperature deposition.

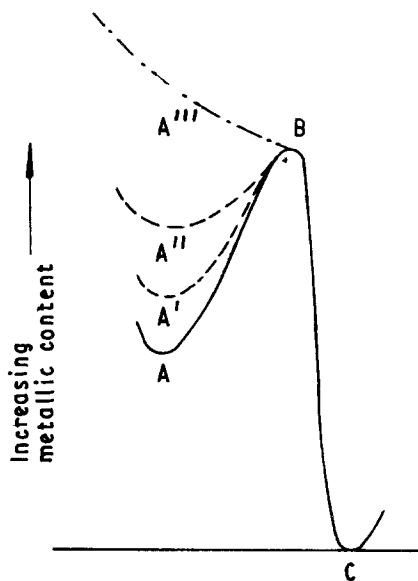


Figure 8 The variation of free energy of the Ge-metallic amorphous alloy phase with C_{Me} .

4.3. The activation energy of crystallization in Ge-metal bilayer films

Because T_c depends not only on the crystallization barrier in the Ge-metal binary films but also on the activation energy, E_a , of crystallization in them, so the influence of the concentration of the alloy film on E_a must be discussed. When the a-c transition is studied, the Johnson-Mehl-Avrami (JMA) equation is usually written as follows [44-49]

$$x = 1 - \exp[-(Kt_{\text{eff}})^n] \quad (3)$$

where x is the volume fraction of transition, t_{eff} is the effective time (annealing time, t_a , minus incubation time, t_0), n is the Avrami exponent, K is the rate constant which is an Arrhenius temperature dependence

$$K = K_0 \exp(-E_a/RT) \quad (4)$$

where the pre-exponential term, K_0 , is the frequency factor, E_a is the activation energy describing the overall crystallization process, R is the gas constant, and T is the absolute temperature. Under our experimental conditions, the annealing time, t_a , is 30 min, the heating rate, R_h , before the counting time and the cooling rate, R_c , after the annealing time, are rapid and roughly the same, the pressure and environment in the quartz tube are in common with each other for each experiment, so we can assume there are no further variations in the formula for E_a except the metallic concentration, C_{Me} , for different alloy films. So the activation energy, E_a , is a single function of C_{Me} , that is, $E_a = E_a(C_{Me})$. E_a usually decreases with increasing C_{Me} with a similar form. Thus the frequency factor, K_0 , and the Avrami exponent, n , are the same for each Ge-metallic film (Equation 3). The difference in the rate constant, K , for example, is only due to the difference in the activation energy, E_a . For Ge-Au (or Ge-Ag) films (Equation 4). Comparing Ge-Au with Ge-Ag films, the values of K_0 and n could be different, but for all the Ge-Au films, which have different C_{Au} ,

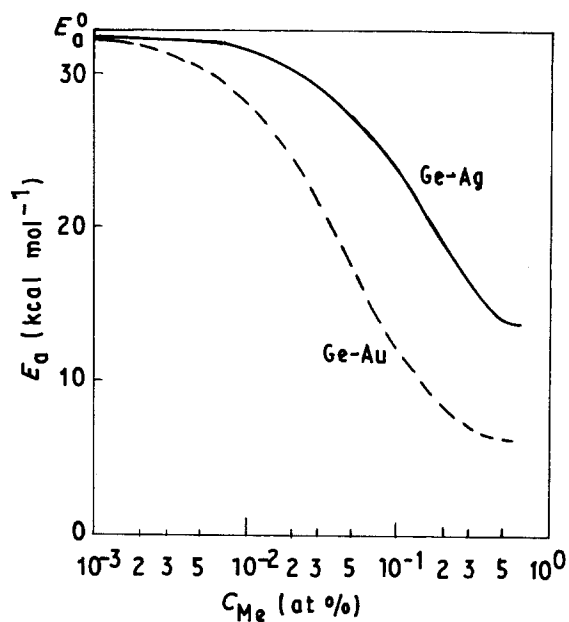


Figure 9 The comparison of E_a of Ge-Au and Ge-Ag alloy films calculated using Equations 5 and 6.

K_0 and n are non-variable. Therefore, we could estimate the values of E_a for Ge-Au and Ge-Ag alloy films using Equations 3 and 4. For the pure a-Ge film, the activation energy of crystallization E_a^0 is $32.5 \pm 2.3 \text{ kcal mol}^{-1}$ ($1.4 + 0.1 \text{ eV}$) [31], which was obtained by differential scanning calorimetry (DSC). Based on the data of the crystallization temperatures, T_c , for different films, and using the least square method of the estimated values of E_a for the films, empirical formulae can be obtained for the two kinds of films

for Ge-Au films

$$E_a(C_{Au}) = E_a^0 / (-18.66C_{Au}^2 + 16.83C_{Au} + 1) \pm 3.3 \text{ (kcal mol}^{-1}) \quad (5)$$

for Ge-Ag films

$$E_a(C_{Ag}) = E_a^0 / (-2.754C_{Ag}^2 + 3.815C_{Ag} + 1) \pm 2.6 \text{ (kcal mol}^{-1}) \quad (6)$$

Fig. 9 is a comparison of E_a - C_{Me} curves for Ge-Au and Ge-Ag alloy films. From this figure we see that the decreased rate for Ge-Au alloy film with increasing gold content is much more rapid than that for Ge-Ag film, coincident with the difference between the T_c s for the two kinds of films. The most popular method used in analysing the crystallization process is differential scanning calorimetry (DSC). However, the most sensitive method for detecting the occurrence of crystallization is electron microscopy (TEM + SAD) [25, 26]. So combining the results of TEM observation and SAD analysis with the value E_a^0 (obtained from the pure a-Ge film with DSC method [31]), we can estimate E_a for the Ge-metallic films which have every metallic concentration in the range of a-Ge crystallization. If the metallic content is larger than the upper limit of the a-c transition for the Ge-metallic system, the activation energy, $E_a(C_{Me})$, of crystallization of the a-Ge-metallic system cannot be obtained. Even in the range of a-Ge crystallization, the situation

could be very complex. For example, the higher metallic content could induce the formation of metastable phase (e.g. Au-Ge metastable phase). During the annealing crystallization process, this metastable phase could dissolve first, then the a-c transition would take place. In this case, E_a obtained by this method would be that for the whole process.

5. Phase diagrams of thin Ge-metallic alloy films

5.1. The first type of phase diagram for binary thin films – the phase formation diagram

When collisions occur between the vapour atoms in the Ge-metallic system and the substrate atoms, and the temperature at the surface of substrate is lower than the glass transition temperature, T_g , the following three independent factors can determine the form of the film, that is, whether or not a stable amorphous film results: (1) the thermodynamic factor which depends on the deposition temperature, T_e , and on the substrate temperature, T_s – this is the basic factor; (2)

the dynamic factor which influences the growth rate of the growing phase in the deposition process (this is discussed for a single component system in [47–49]); (3) for the alloy films, we believe that the atomic composition is an important factor [25, 26]. For example, if the growing phase of the Ge-metal alloy film is the a-Ge phase, then the metallic atomic concentration in the ambient area could be higher than that in the growing phase, perhaps another phase may be formed, and then the layer structure could form, therefore the final film structure formed could be influenced by this factor. The above factors are inter-related with each other with certain roles.

Gutzow and Avramov [47–49] presented phase formation diagrams for the pure element films (see Fig. 10a and b). In order to investigate the relationship of phase formation in Ge-metal alloy films under vacuum deposition we have expanded it for the case of semiconductor-metal alloy films, so that a three-dimensional phase formation diagram is obtained (Fig. 10c). The three coordinate axes of the phase diagram are the relative substrate temperature T_{er} (x -axis), the relative vapour temperature, T_{vr} (y -axis), and the atomic composition, C_{mr} (z -axis) (Fig. 10). The

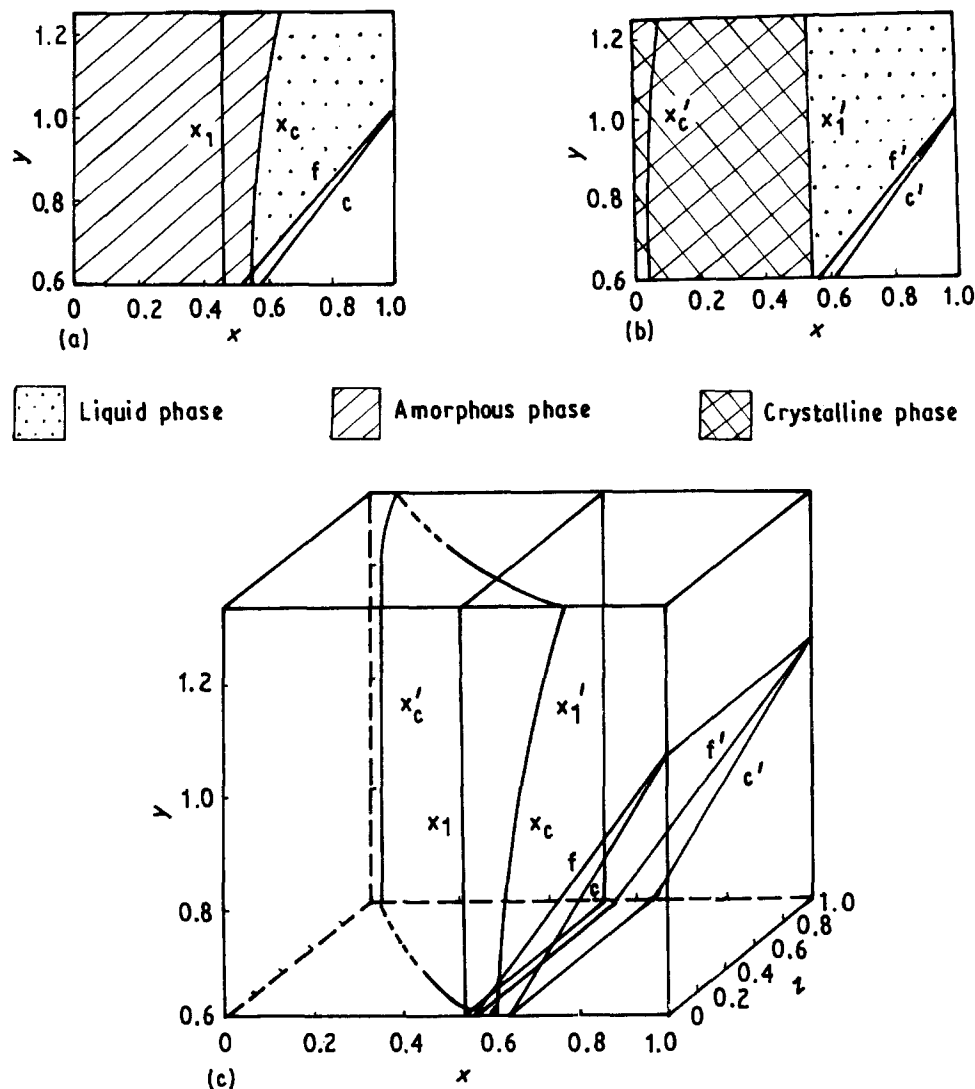


Figure 10 The first type of phase diagram of a thin film, the phase formation diagram. (a) Pure semiconductor (Ge or Si) film; (b) pure metallic film; (c) semiconductor-metal alloy film.

definitions of T_{er} , T_{vr} and C_{mr} are

$$T_{er} = \frac{T_s}{T_m} \quad (7)$$

$$T_{vr} = \begin{cases} \frac{T_c}{T_m} & T_e < T_m \\ \frac{T_c}{T_m} \frac{1 - \lambda_m/\lambda_c}{1 - \lambda_m T_c/\lambda_c T_m} & T_e > T_m \end{cases} \quad (8)$$

$$C_{mr} = \frac{C_m}{\sum_i C_i} \quad (9)$$

where T_m is the melting point for the infinite bulk alloy, λ_m and λ_c are, respectively, the melting heat and the sublimation heat of the alloy under condensation conditions, C_m is the metallic composition and C_i the i th element composition.

Fig. 10a (plane $z = 0$ in Fig. 10c) represents the phase formation diagram of the pure semiconductor; Fig. 10b (the plane $z = 1.0$ in Fig. 10c) is the phase formation diagram of the pure metal; the surfaces ff' and cc' in Fig. 10c are the melting and solidification curved surfaces, respectively. Assume r_1 is the radius of the smallest atomic cluster when the difference between the liquid state and the crystalline state can just be detected, r_m is the radius of the atomic cluster when the melting just continues on the surface of the substrate, then the surface $x_1x'_1$ is the curved surface which satisfies the condition $r_1 = r_m$. Also assume T_c^o is the critical temperature at which the alloy system can form the amorphous state, then the surface $x_cx'_c$ is the curved surface which satisfies the condition of amorphous phase formation. Based on the theoretical calculation of T_c^o [25, 26]

$$T_c^o = - \frac{U(r)}{R \ln(c_2 z_v d^2)} \quad (10)$$

where z_v is the collision frequency of the vapour atoms with the substrate, d is the equilibrium atomic distance, $U(r)$ is the relaxative activation energy of the atomic cluster which has the radius r , R is the gas constant, c_2 is another constant. Because the different kinds of atom can accelerate the atomic diffusion in the alloy system, $U(r)$ and T_c^o decrease with increase of C_{Me} in the Ge-metallic films in the same way.

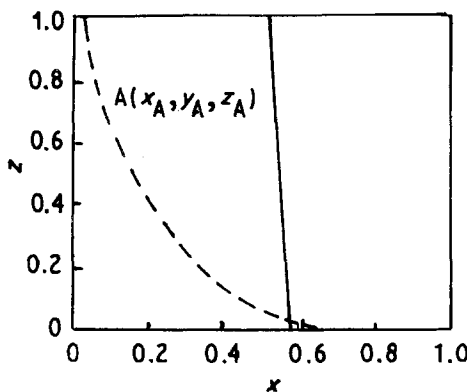


Figure 11 The horizontal section of the phase formation diagram for Ge-metal alloy film under vacuum deposition.

Fig. 11 is the phase formation diagram of the alloy system at a given temperature; it is a horizontal section of the diagram in Fig. 10c. From point A in this figure we know that when the relative substrate temperature is x_A and the relative vapour temperature is y_A , the maximum metallic content is $z_A = C_{max}$ at which the amorphous state just occurs under vacuum deposition conditions. It should be noted that, because the properties of the alloy system near the eutectic point are very complex, further information and analysis are required before the diagram can be defined exactly, so the lines in this region are dashed.

5.2. The second type of phase diagram for binary thin films – the phase transition diagram

When the alloy films deposited at room temperature are annealed in vacuum, the phase composition in the film varies with annealing temperature, T_a , and the a-c transition could take place if the annealing temperature, T_a , is high enough. This is a non-equilibrium problem. Although the T_a curves can be marked in the Ge-metal equilibrium phase diagram (Fig. 6), it is insufficient for describing the structural character of the phase composition for thin films. In order to describe the character of the phase transition of thin films in vacuum annealing, a second type of phase diagram for thin films is introduced, that is, the three-dimension phase transition diagram. The main factors which influence the phase transition character are as follows: (1) the deposition temperature, which determines the energy situation of deposited films; (2) the annealing temperature, which determines the energy variation of the deposited films; and (3) the metallic concentration C_{Me} . Fig. 12 shows the three-dimension phase diagram, the three coordinate axes of the diagram being the relative vapour temperature, T_{vr} (or the relative substrate temperature T_{er} , x-axis), the relative annealing temperature, T_{ar} (y-axis), and the atomic composition, C_{mr} (z-axis). The definition of the T_{ar} is

$$T_{ar} = \frac{T_a}{T_{cu}} \quad (11)$$

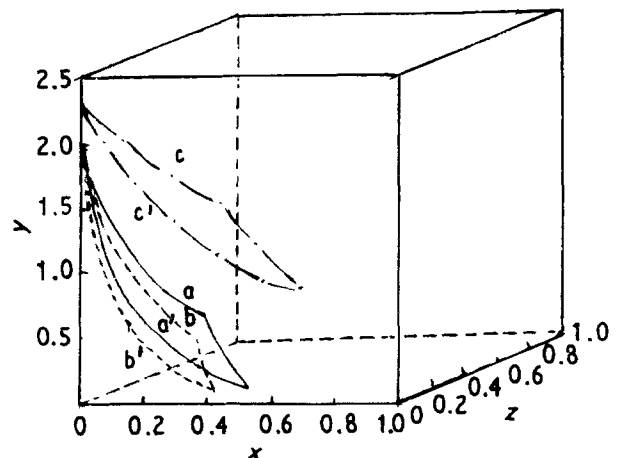


Figure 12 The second type of phase diagram of a thin film. (—) a-c (or m-c) transition, (---) a-c transition, (-·-) s-l transition.

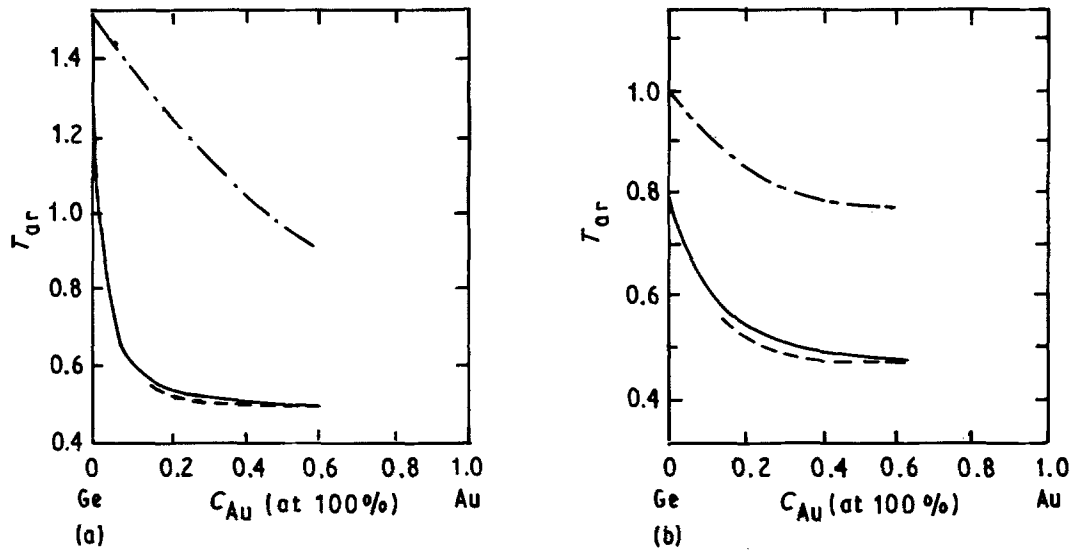


Figure 13 The phase diagram for vacuum annealed Ge-metal alloy films. (a) Ge-Au, (b) Ge-Ag. (—) a-c (or m-c) transition, (---) a-m transition, (-·-) s-l transition.

where T_{eu} is the eutectic temperature of the amorphous semiconductor-metal system. The definitions of T_{vr} (or T_{er}) and C_{mr} are shown in Equations 8 and 9. The surfaces aa' , bb' and cc' in Fig. 12 are the a-c transition, amorphous phase-metastable phase transition and crystalline phase-liquid phase transition curved surfaces, respectively. The horizontal plane at $T_{ar} = 0$ in Fig. 12 is the same as the vertical plane at $T_{er} = \text{constant}$ in Fig. 10.

Fig. 13a and b are the two-dimensional cross-sections of this kind of phase diagram for Ge-Au and Ge-Ag thin films (schematic representation); these cross-sections are the T_{ar} - C_{Me} diagrams. It can be seen from Fig. 13 that the a-c transition curves have almost the same shape for the Ge-Au and Ge-Ag systems. When the metallic content is higher, the values of T_{ar} for the a-c transition are near 0.5 for the two systems. The dashed curves in the diagrams indicate the metastable phase transition. It is slightly lower than that of the a-c transition. When the annealing temperature is high enough, the alloy film could melt. The melting line could fall with the increasing metallic content. If we change the deposition temperature by changing the deposition voltage, it is found that the higher the deposition temperature of the alloy films, the lower the crystallization temperature, T_c , of a-Ge in the alloy films [50]. We also changed the substrate temperature, T_s , and found that if the film is deposited on a hot NaCl monocrystalline substrate ($T_s = 200^\circ\text{C}$), the value of T_c decreases [50]. If we want to describe this situation, the three coordinate axes can be selected as T_{er} - T_{ar} - C_{mr} . It is indicated that a-Ge is in a more unstable situation for the higher deposition temperature and higher substrate temperature, the crystallization barrier for the Ge-metal system decreases, so T_c also decreases.

6. Comparison of T_c of binary films with bilayer films

Semiconductor-metal bilayer films also have many applications in the field of electrical devices. The

crystallization properties for this kind of film (Ge-Au and Ge-Ag bilayer films) have also been studied by us [25, 26, 50]. From the Ge-Au and Ge-Ag equilibrium phase diagrams which are represented in Fig. 6 it is known that the T_c of the a-Ge/p-Au film (100°C , 373 K) is almost equal to that of the Ge-(10-15 at%) Au film, and T_c of the a-Ge/p-Ag film (280°C , 553 K) is almost equal to that of the Ge-18 at% Ag film. When the metallic content in the amorphous alloy film is lower than the critical value mentioned above, T_c is higher than that of the bilayer film; otherwise, when C_{Me} is higher than the critical value, T_c is lower than that of the bilayer film. It must be recognised for the correct explanation of this phenomenon, that there are different crystallization mechanisms for these two kinds of film.

It has been pointed out that [25, 26, 50]: (1) the grain-boundary triple points in the polycrystalline metallic film are favourable nucleation positions for a-Ge crystallization in the a-Ge/p-Au films; (2) the local regional rapid crystallization for the a-Ge takes place in the aggregation regions during the annealing process, the favourable crystallization regions in the a-Ge/p-Au films are related to the voids of the annealed p-Au films. Because of these two reasons, the T_c of the a-Ge in the a-Ge/metallic bilayer film drops to a value which is much lower than that of the pure a-Ge film. If the a-Ge crystallization barrier decreases and the activation energy of crystallization increases, the crystallization temperature, T_c , decreases. The experimental results for a-Ge alloy films have shown that when metallic content, C_{Me} , in the amorphous alloy films is lower, the accelerated action is smaller than that caused by the decrease of the critical nucleation work caused by the grain-boundary triple points in the bilayer films; but when the metallic content is higher, on the one hand the decrease of the crystallization barrier and the increase of the crystallization activation energy are more obvious, but on the other hand the metallic grains, which are introduced during the deposition process, can provide many grain-boundary triple points, their promoted action for the

c-Ge nucleation and growth also has an important influence on the a-Ge crystallization, so that T_c for the binary alloy film is lower than that of the bilayer film.

7. Conclusions

From the systematic TEM observations and SAD analyses for the Ge–Au and Ge–Ag co-deposited films in vacuum at room temperature, and their annealed films, the following conclusions can be drawn.

1. For the semiconductor–metal deposited films, the structure is determined by the metallic content: when the metallic content is smaller than a certain value, C_{\max} , the film may be amorphous; otherwise the film is crystalline. A new formula for C_{\max} is derived.

2. The annealed crystallization temperature, T_c , decreases with increasing C_{Me} , when $C_{\text{Au}} > 15$ at% or $C_{\text{Ag}} > 18$ at%, T_c is lower than that for a-Ge/poly-crystalline metal bilayer films.

3. In the gold-rich alloy films before a-Ge crystallization, the metastable alloy phase resolves first, the crystallized film being composed of the c-Ge and c-Au phases. For the Ge–Ag alloy films, the situation is more complex. In the Ag-rich alloy film, as T_a increases, the Ag–Ge metastable phase forms first, then this phase dissolves and a-Ge crystallizes in the alloy film.

4. The variation of crystallization barrier and the activation energy of crystallization determine the variation of T_c with the metallic contents, C_{Me} . The activation energy, E_a , of crystallization for Ge–Au and Ge–Ag films can be obtained from the data of T_c by TEM observations and SAD analyses. $E_a = E_a^0 / (-18.66C_{\text{Au}}^2 + 16.83C_{\text{Au}} + 1) \pm 3.3$ (kcal mol⁻¹) for Ge–Au films; $E_a = E_a^0 / (-2.754C_{\text{Ag}}^2 + 3.815C_{\text{Ag}} + 1) \pm 2.6$ (kcal mol⁻¹) for Ge–Ag films.

5. The first type of three-dimensional phase diagram for phase formation is introduced for binary alloy films in order to determine the phase constitution; this diagram has three axes representing the three principal factors influencing phase formation: thermodynamic, dynamic, and composition factors.

6. A second type of three-dimensional phase diagram for describing the phase transition is also proposed. Using this kind of phase diagram the a–c transition and the transition from a metastable phase to a stable crystalline phase can be investigated in detail.

Acknowledgement

The assistance of Ms Y. Wang, X. Zhang, X. Gai and J. Zhang in the electron microscope laboratory at Beijing University is gratefully acknowledged. This work was supported by the ZhongGuanCun Analytical Foundation of Beijing, Peoples' Republic of China.

References

1. W. BUCKEL, *J. Vac. Sci. Technol.* **10** (1973) 599.
2. Ph. MANGIN, G. MARCHAL, C. MOUREY and Chr. JANOT, *Phys. Rev.* **B2** (1980) 3047.

3. SUICU LO, DACHEN QING and ZIQIN WU, *Phys. Sinica* **31** (1982) 1401 (in Chinese).
4. A. GHEORGHIN, K. DRICC-KHODJA, S. FISSON, M. L. THEYE and J. DIXMIER, *J. Phys. Colloq.* **46** (1985) C8, 545.
5. A. C. ZETTMLOYER, in "Proceedings of the Conference on Ohmic Contact to Semiconductors", Montreal, Canada (1968) p. 48.
6. K. L. CHOPRA, P. NATH and A. C. RASTOGI, *Phys. Status Solidi* **A27** (1975) 645.
7. K. L. CHOPRA and P. NATH, *ibid.* **A33** (1976) 333.
8. K. L. CHOPRA, H. S. RANDHAWA and L. K. MALHOTRA, *Thin Solid Films* **47** (1977) 203.
9. P. NATH, V. DUTTA and K. L. CHOPRA, *ibid.* **64** (1979) 65.
10. P. NATH and K. L. CHOPRA, *ibid.* **58** (1979) 339.
11. P. NATH, V. DUTTA and K. L. CHOPRA, *J. Phys. C. (GB)* **12** (1979) L203.
12. *Idem*, *Phys. Status Solidi* **A34** (1976) 405.
13. V. DUTTA, P. NATH, V. D. VANKAR and K. L. CHOPRA, *ibid.* **A49** (1978) 379.
14. H. S. RANDHAWA, L. K. MALHOTRA and K. L. CHOPRA, *J. Appl. Phys.* **49** (1978) 4294.
15. H. S. RANDHAWA, P. NATH, L. K. MALHOTRA and K. L. CHOPRA, *Sol. Stat. Commun.* **21** (1976) 73.
16. *Idem*, *J. Non-Cryst. Solids* **29** (1978) 311.
17. *Idem*, *Phys. Status Solidi* **A37** (1976) 313.
18. N. G. NAKHODKIN, A. I. NOVOSEL'SKAYA and A. F. BARDAMID, *Sov. Phys.-Semicond.* **19** (1985) 1182.
19. Y. SAITO, *J. Phys. Soc. Jpn* **53** (1984) 4230.
20. T. B. LIGHT and C. N. J. WAGNER, *J. Appl. Crystallogr.* **1** (1968) 199.
21. J. S. JOHANNESSEN, in "Proceedings of the 4th Nordic Solid State Conference", Turku, Finland (1970) p. 53.
22. S. SHIMAOKA and S. C. C. CHANG, *J. Vac. Sci. Technol.* **8** (1971) 243.
23. *Idem*, in "Proceedings of the 28th Electron Microscopy Society of America", Houston, USA (1970) p. 512.
24. M. L. THEYE, *Mater. Res. Bull.* **6** (1971) 103.
25. RENJI ZHANG, SHENGLING CHU and ZIQIN WU, *Phys. Sinica* **35** (1986) 365 (in Chinese).
26. *Idem*, *Chinese Phys. Lett.* **2** (1985) 211.
27. B. PREDEL and D. W. STEIN, *Z. Naturforsch.* **A26** (1971) 722.
28. A. BARNA, P. B. BARNA and J. F. POCZA, *J. Non-Cryst. Solids* **8–10** (1972) 36.
29. N. G. NAKHODKIN, A. F. BARDAMID, A. I. NOVOSEL'SKAYA and K. I. YAKIMOV, *Sov. Phys. Solid State* **29** (1987) 410.
30. F. YOGAWA and Y. FUJIKI, *J. Appl. Phys. Jpn* **8** (1969) 1056.
31. P. GERMAIN, K. ZELLAMA, S. SQUELARD, J. C. BOURGOIN and A. GHEORGHIN, *J. Appl. Phys.* **50** (1979) 6986.
32. A. G. FITZGERALD, *J. Mater. Sci. Lett.* **1** (1982) 145.
33. RENJI ZHANG, YUPING WANG and ZIQIN WU, *J. Chinese Elect. Micros. Soc.* **3(4)** (1984) 69.
34. *Idem*, in "Proceedings of the Beijing Conference and Exhibition of Instrumental Analysis" ed. C. C. Gus Vol. 1 (1985) p. 83.
35. G. W. RACKHOM and J. W. STEEDS, *Inst. Phys. Conf. Ser.* **41C** (1978) 178.
36. K. TAMURA, J. FUKUSHIMA, H. ENDO, K. KISHI, S. IKEDA and S. MINOMURA, *J. Phys. Soc. Jpn* **36** (1978) 565.
37. G. SCHLUCKEBIER and B. PREDEL, *Z. Metallkde* **71** (1980) 535.
38. M. K. GARDINER, D. COLBOURNE and C. NORRIS, *Philos. Mag.* **B54** (1986) 133.
39. H. NEUMANN, W. OYER, A. G. ILIUSKII, T. M. KHRISTENKO, L. E. MIKHAILOVA, A. V. ROMANOVA, T. SCHOLZ and M. WOBST, *Wiss. Z. Tech. Univ. Karl-Marx-Stadt* **29** (1987) 306.
40. D. TURNBULL, *Contemp. Phys.* **10** (1969) 473.
41. D. TURNBULL and P. E. POLK, *J. Non-Cryst. Solids* **8–10** (1972) 19.
42. H. S. CHEN and D. TURNBULL, *Acta Metall.* **17** (1969) 1021.
43. *Idem*, *Contemp. Phys.* **10** (1969) 473.

44. C. ORTIZ, K. A. RUBIN and S. AJURIA, *J. Mater. Res.* **3** (1988) 1196.
45. Y. Q. GAO and W. WANG, *J. Non-Cryst. Solids* **81** (1986) 129.
46. E. POCZA, *J. Vac. Sci. Technol.* **6** (1969) 472.
47. I. GUTZOW and I. AVRAMOV, *J. Non-Cryst. Solids* **16** (1974) 128.
48. *Idem*, *Thin Solid Films* **85** (1981) 203.
49. I. AVRAMOV and I. GUTZOW, *ibid.* **185** (1990) 91.
50. RENJI ZHANG, LILI and ZIQIN WU, *ibid.* **208** (1992) 295.
51. K. KIM and D. D. L. CHANG, "Thin Films-Interfaces and Phenomena", Fall Meeting, Boston, USA (1985) p. 437.
52. S. R. HERD, P. CHAUDHARI and M. H. BRODSKY, *J. Non-Cryst. Solids* **7** (1972) 309.
53. M. HAFIZ, E. MGBENU, P. A. TOVE, H. NORDE and S. PETERSSON, *Vacuum (GB)* **27** (1977) 193.
54. G. Y. ROBINSON, *Thin Solid Films* **72** (1980) 129.
55. V. M. DENISOV, V. V. BELETSKII and P. M. SHURYGIN, *Inorg. Mater.* **23** (1987) 298.

*Received 29 January 1991
and accepted 19 February 1992*